Supplementary Materials

Void bias in irradiated model metals

Ziang Yu, Haixuan Xu

Department of Materials Science and Engineering, University of Tennessee, Knoxville, TN 37996, USA.

Correspondence to: Prof. Haixuan Xu, Department of Materials Science and Engineering, University of Tennessee, 336 Ferris Hall, 1508 Middle Drive, Knoxville, TN 37996-2100, USA. E-mail: xhx@utk.edu

I. Point defect lifetime vs. KMC simulation system size

Point defect lifetime vs. KMC simulation system size data for both interstitials and vacancies in Fe, Cu, and Ni are provided in Fig. S1. The system sizes used in KMC simulations correspond to number densities near 10^{22} m^{-3}, which is higher than typical void densities observed in experiments. Defect lifetimes with lower void densities were extrapolated from fits to these raw data.

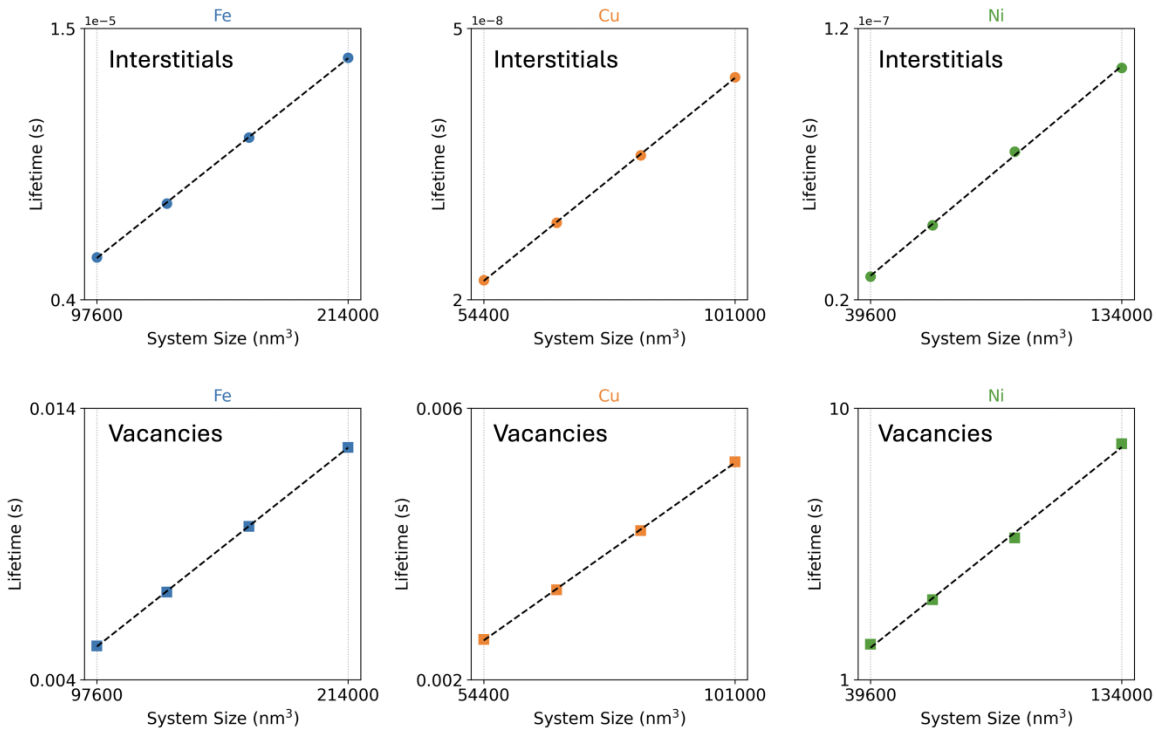

Figure S1. Interstitial lifetime (top row) and vacancy lifetime (bottom row) as a function of simulation system size for (first column) Fe, (second column) Cu, and (third column) Ni.

II. Standard error of lifetime

For a given void size, density, and temperature, a KMC simulation is performed with 500 randomly selected starting positions and 4000 trajectories, balancing calculation efficiency and accuracy. Starting positions refer to where the point defect is introduced for the KMC simulations. We introduce one point defect at each starting position and perform 4000 KMC calculations independently. Here in the figure, we provide the interstitial lifetime standard error with a void density at 10^{22} m^{-3} at 573 K. In this case, the mean value of interstitial lifetime is $5.8*10^{-6}$ s.

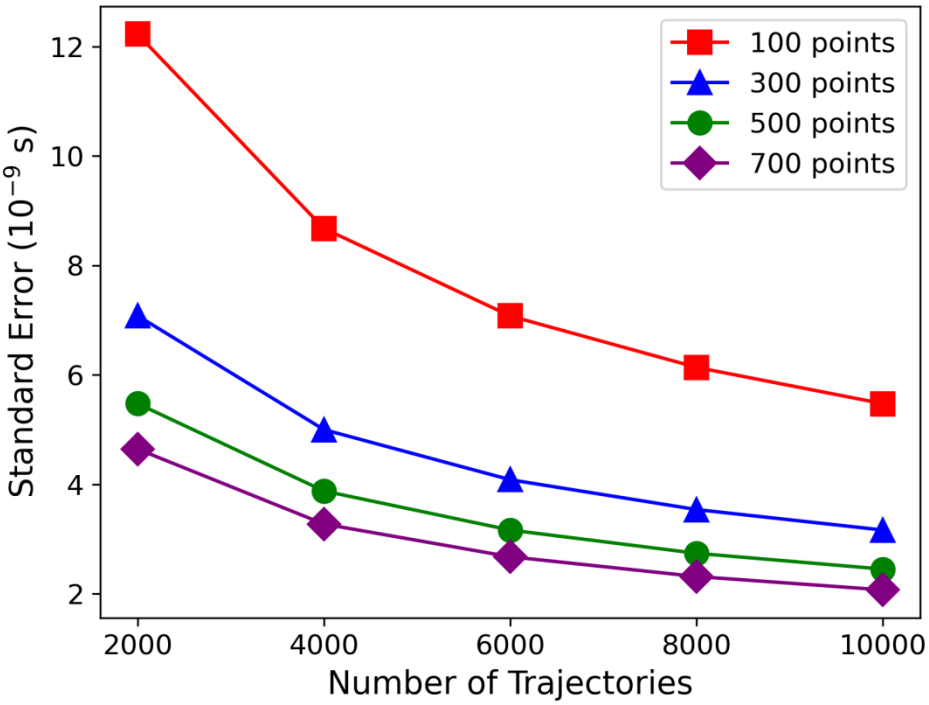

Fig. S2. Interstitial lifetime standard error with various starting positions and number of trajectories.

III. Migration energy barriers (MEBs) and the core effect of voids in Cu and Ni

The void core effect, along with the MEBs in irradiated Fe is presented in the main body of the article. As a reference, Fig. S3 and S4 illustrate the MEBs of a [100] dumbbell as a function of positions near a 10 nm void in irradiated Cu and Ni, respectively. The MEBs in the core region are calculated using self-evolving atomistic kinetic Monte Carlo (SEAKMC) [1,2], while the MEBs in outer regions are estimated using the dipole tensor method [24, 25]. MEBs in Cu and Ni also exhibit strong anisotropy due to the atomistic interaction between mobile point defects and voids within the core regions, comparable to those in Fe. The spontaneous absorption regions are approximately 2 nm from the void surface in both fcc Cu and Ni.

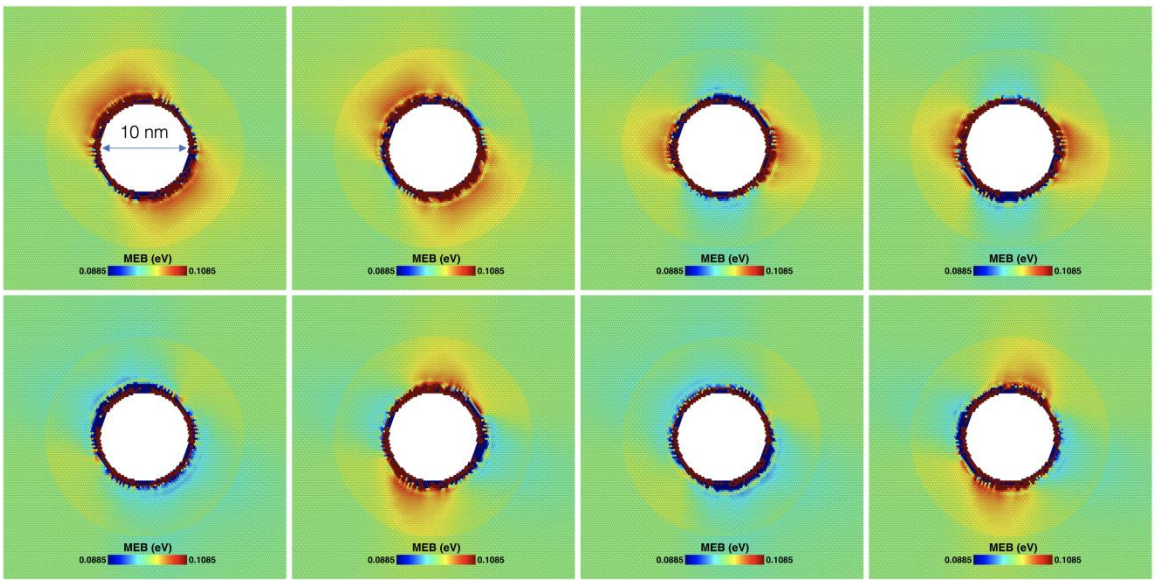

Fig. S3. MEBs of a [100] dumbbell in irradiated Cu around a 10 nm loop. Eight saddle points to four first nearest neighbors (1NN) are presented. The core regions (in dark red and blue) are around 2 nm in width, similar to those in Fe.

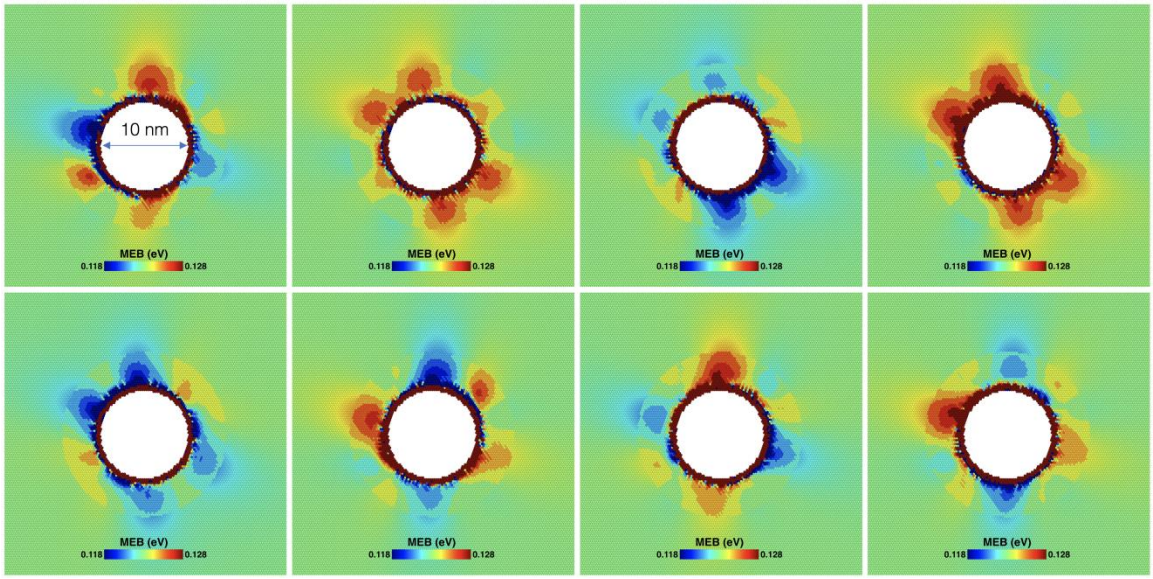

Fig. S4. MEBs of a [100] dumbbell in irradiated Ni around a 10 nm loop. Eight saddle points to four first nearest neighbors (1NN) are presented. The core regions (in dark red and blue) are around 2 nm in width, similar to those in Cu and Fe.

IV. Void morphology effect

Voids have traditionally been assumed to be spherical defect clusters in theoretical studies. However, experimental observations show that void shapes vary [3-6]. The varying morphology can impact the stress/strain field around voids, subsequently influencing the interactions with

mobile point defects and resulting in different void biases. To examine the void morphology effect, this study considered two distinct shapes based on experimental observations. For the comparison with the spherical void in bcc Fe (Fig. S5a), a cubic void with a 4 nm edge in bcc Fe (Fig. S5b) is introduced. Similarly, for the comparison with the spherical void in Cu (Fig. S5c), a truncated octahedron void spanning 4 nm between its diagonal vertices (Fig. S5d) is provided. The bias of each void shape is presented in Table SI, along with specific bias values to mitigate the size effect. Notably, voids can assume a wide variety of shapes in reality due to atomic-scale irregularities and other external conditions. The chosen shapes are typical under TEM observations and are able to provide insight into fundamental interactions, providing a conceptual understanding of the void morphology effect.

The interactions between point defects and voids with different shapes exhibit relatively minor variations based on strain fields. For instance, both compressive and tensile regions are positioned similarly for the spherical and cubic voids in bcc Fe, as shown in Fig. S5a and S5b. However, the compressive regions around cubic voids are relatively larger near the void surface, compared with compressive regions of spherical voids. This enhances the absorption of vacancies and subsequently decreases the bias for cubic voids. In bcc Fe, the bias of cubic voids is slightly higher (around 0.05) than that of a spherical void with a comparable size (~ 4 nm) from 573 K to 673 K with a density of 10^{20} m^{-3}, as given in Table SI. Comparatively, the primary strain field differences with spherical and truncated octahedron shapes in Cu, as depicted in Fig. S5c and S5d, are not as obvious as that in Fe, resulting in a smaller difference of bias values between these two shapes (around 0.03). Based on these results, the morphology effect is not as significant as the size effect. It is challenging to make a further quantitative comparison among different void shapes using conventional parameters, since the number of vacancies contained within voids of different shapes varies. The specific bias of voids with different shapes is presented in Table SI, demonstrating that the influence of void shapes is less significant compared to the effects of sizes and sink types. In general, for voids with an approximate size of 4 nm, the specific bias is between 10^{-4} and 10^{-5}. The difference in specific bias caused by void shapes is less than $2*10^{-5}$ in both Fe and Cu. This finding indicates that void shapes insignificantly affect the void swelling calculations. Additionally, the specific bias for 4 nm voids in Cu is higher than that in Fe, regardless of whether the voids are spherical, cubic, or truncated octahedrons. Consequently, together with the evolving shapes of voids during irradiation experiments, we consider spherical voids to be statistically representative for void swelling calculations.

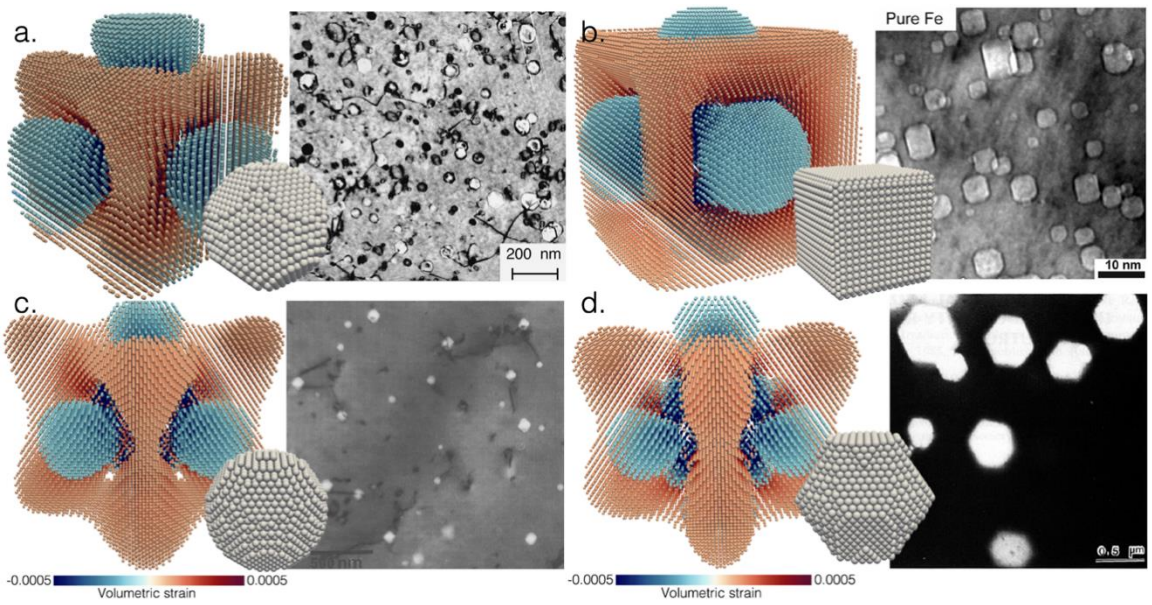

Fig. S5. Void strain fields and atomic structures with different shapes based on experimental observations [3,5,7,8] for (a) Spherical void in Fe, (b) cubic void in Fe, (c) spherical void in Cu, and (d) truncated octahedron void in Cu. Sizes are approximately 4 nm to facilitate direct comparisons with spherical voids. Reprinted with permission from Refs. [3,5,7,8].

Table SI. Shape effect on void bias of unit volume in bcc Fe and fcc Cu. The size of voids is ~4 nm (diameter for spherical voids and edge length for cubic voids). The number density is set to be 10^{20} m^{-3}. Spherical voids respectively contain 2891 vacancies in Fe and 2796 in Cu, the cubic void in Fe contains 6119 vacancies, and the truncated octahedron void in Cu contains 2685 vacancies. The Specific bias is discussed in Section III.

	Bias			Specific bias (10^{-5})		
Temperature (K)	573	673	773	573	673	773
Spherical void (Fe)	0.124	0.117	0.116	4.27	4.03	4.01
Cubic void (Fe)	0.172	0.161	0.143	2.81	2.63	2.33
Spherical void (Cu)	0.211	0.191	0.183	7.85	7.11	6.8
Truncated octahedron void (Cu)	0.249	0.234	0.216	9.27	8.72	8.04

V. Capture efficiencies of interstitials and vacancies in Fe, Cu, and Ni at 573 K

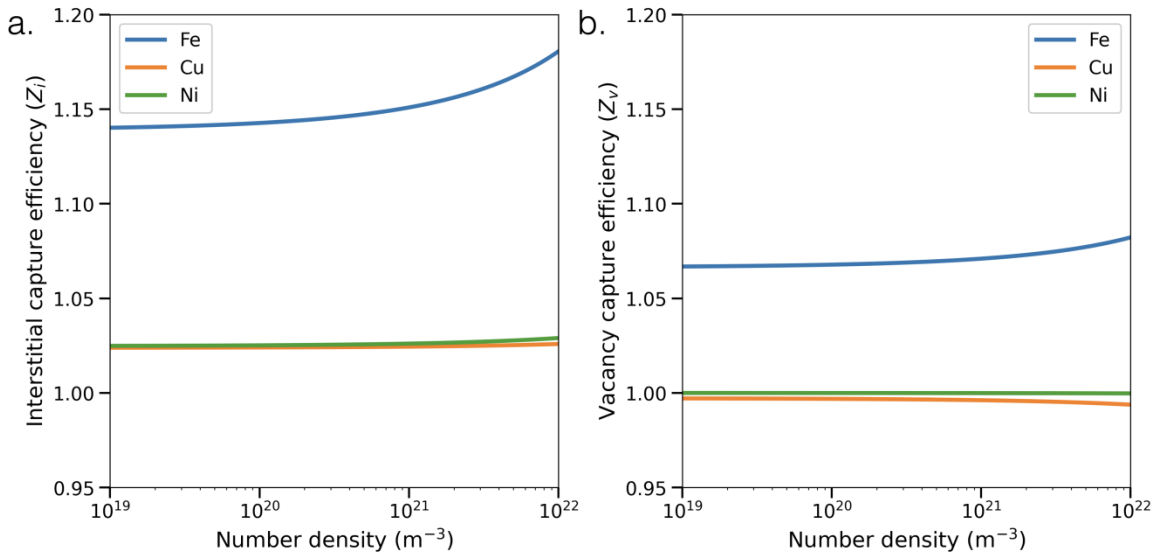

Figure S6. Capture efficiencies of (a) interstitials and (b) vacancies in Fe, Cu, and Ni at 573 K. The void size is 10 nm.

VI. Swelling rate calculation

We consider recombination and thermal emissions separately while calculating the swelling rate. Considering the correlated defect recombination, a survival fraction at 0.1 [9] is multiplied by the obtained swelling rate $\frac{dS}{d\phi}$. Additionally, vacancy evaporation has been considered for 10 nm voids, with evaporation rates exceeding 60% at 773 K. Since the evaporation rate is proportional to the void size, this phenomenon is negligible in very small voids and shrinking voids. Following Golubov et al. [10], the swelling rate is,

$$Swelling\ rate = \varepsilon * \frac{dS}{d\phi} * \left(1 - \frac{J_v^{em}}{N}\right).$$

J_v^{em} is the vacancy emission rate [10,11],

$$J_v^{em} = \frac{D_v C_v^{eq}}{\Omega} 4\pi R,$$

where D_v is the diffusion coefficient of vacancies, Ω is the atomic volume, R is the radius of the void, and C_v^{eq} is the vacancy equilibrium concentration, which is given by

$$C_v^{eq} = \exp\left(-\frac{E_b}{k_B T}\right),$$

where E_b is the binding energy of a vacancy with a void. The binding energies are calculated as the average of the values obtained at each atomic site on the void surface using LAMMPS. R values are obtained from experimental observations as a function of temperature.

VII. Dipole tensor method

For dipole tensor calculations, the migration energy barrier (MEB) and local elastic strain tensor for a dumbbell is obtained using this equation [12]:

$$E^m[\varepsilon]=E_0^m+P_{ij}^{ini}\varepsilon_{ij}(\vec{r}_{ini})-P_{ij}^{sad}\varepsilon_{ij}(\vec{r}_{sad})$$

$$P_{ij}=-V<\sigma_{ij}>.$$

Here, ε_{ij} is the strain tensor, E^m is the MEB with elastic interaction, while E_0^m is the migration energy without elastic interaction (bulk value, 0.308 eV, 0.099 eV, and 0.123 eV for interstitials in and 0.640 eV, 0.693 eV, and 1.036 eV for vacancies in Fe, Cu, and Ni, respectively). The elastic dipole tensors at its initial stable position $\vec{r}_{ini}$ and the saddle point $\vec{r}_{sad}$, P_{ij}^{ini} and P_{ij}^{sad}, are calculated using a supercell. P_{ij} works with fixed periodicity vectors between the defective and original supercells, where V is the volume of the supercell and σ_{ij} is the residual stress.

Detailed data is obtained using the MD simulation in a cubic box (30*30*30 a^3), performed by LAMMPS and shown in the following Table SII. Note that we need to calculate six dumbbell configurations for Fe and three dumbbell configurations for Cu and Ni, as well as the vacancy for all metals. We calculate the dipole tensor for the defect at the relaxed configuration as well as the defect at the saddle point configuration with details shown in the following Table SII.

Table SII. The dipole tensor P_{ij} of point defects in bcc Fe using different interatomic potentials. We take the saddle point between a vacancy and its 1NN vacancy along [111] direction as an example for vacancies, and the saddle point between a [110] dumbbell (**DB**) and its 1NN [011] dumbbell along [111] direction as an example for dumbbells. The dipole tensors of the other migration directions are operated by the symmetry of the defect configuration.

Fe		P_{xx}	P_{yy}	P_{zz}	P_{xx}	P_{xz}	P_{yz}
This work [a]	**Vacancy**	-1.749	-1.749	-1.749	-1.784	-1.784	-1.784
	[110] DB	1.358	0.042	-1.806	-0.627	0.940	3.089
Hao [b]	**Vacancy**	-1.805	-1.805	-1.805	-1.809	-1.809	-1.809
	[110] DB	1.286	-0.031	-1.880	-0.629	-0.940	3.088
DFT *	**Vacancy** [c]	-0.294	-0.294	-0.294	-1.549	-1.549	-1.549
	[110] DB [d]	2.1535	0.8535	-2.532	-2.122	-0.6	3.0

VIII. MEBs of a 10 nm void in Cu and Ni

The MEB around a 10 nm void and 4 nm void in bcc Fe have been provided in the main body of the article. Here, the void MEBs in fcc Cu (10 nm, 4 nm) and Ni (10 nm, 4 nm) are provided from Fig. S7 to Fig. S10. Note that the MEBs close to bulk values are hidden.

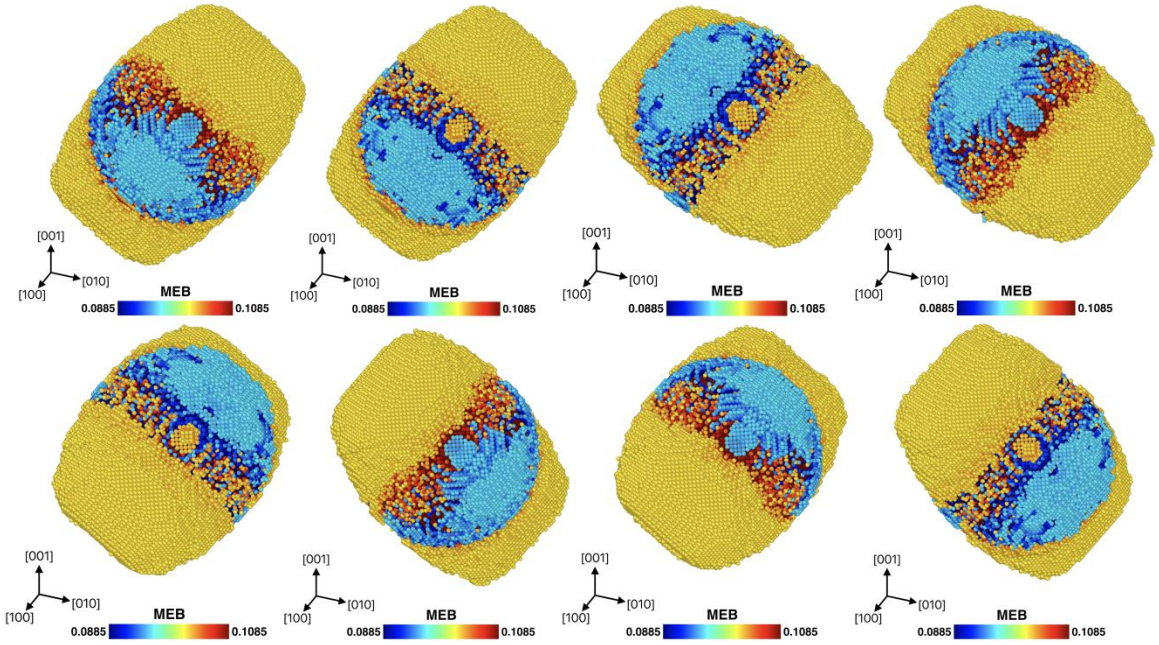

Fig. S7. MEBs of a 10 nm void in fcc Cu.

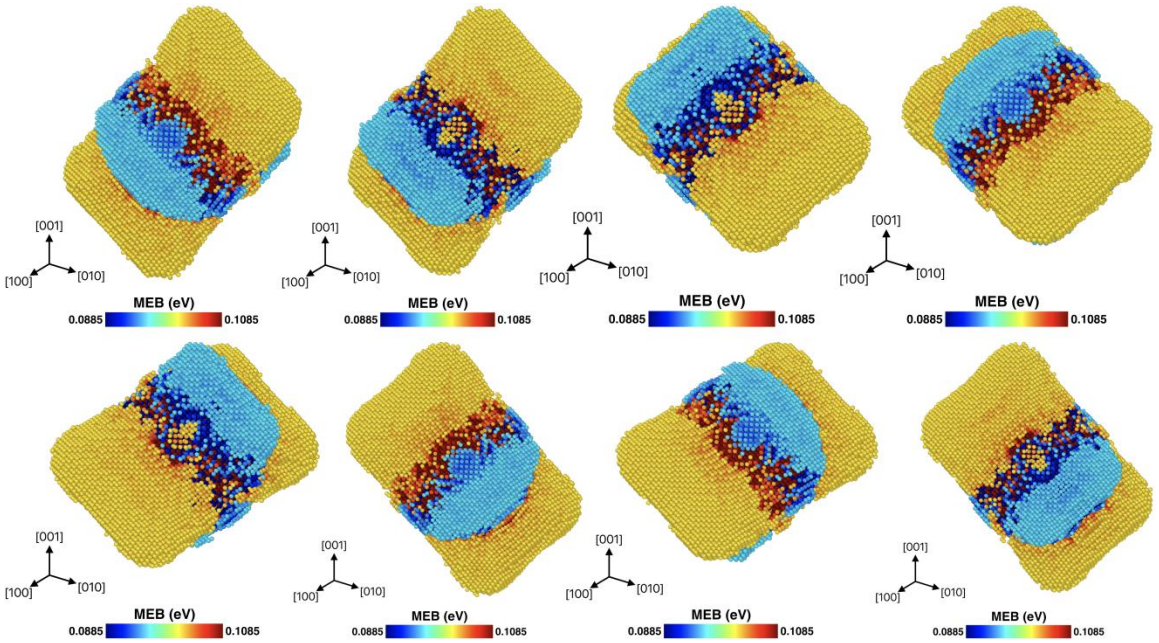

Fig. S8. MEBs of a 4 nm void in fcc Cu.

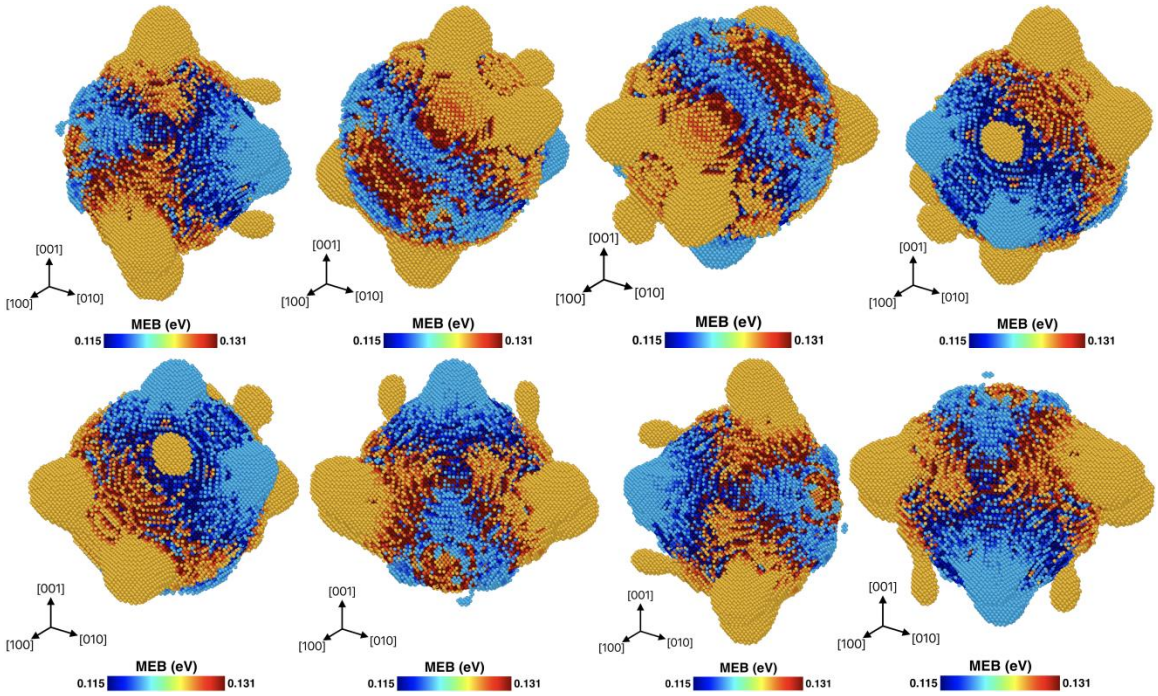

Fig. S9. MEBs of a 10 nm void in fcc Ni.

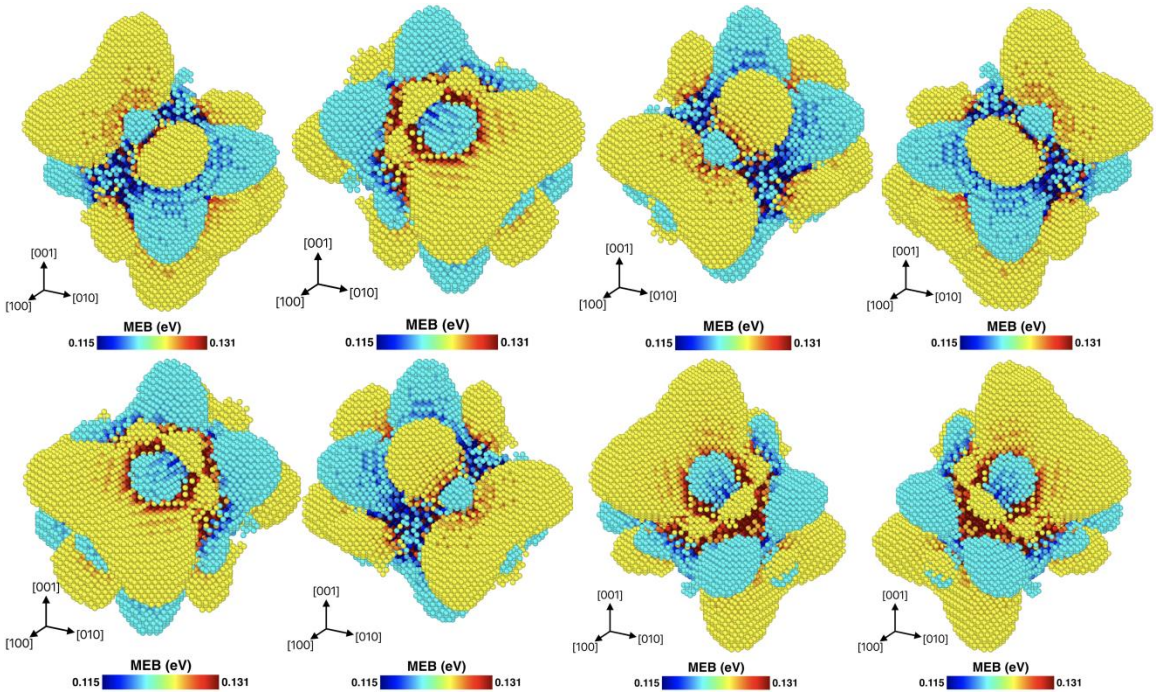

Fig. S10. MEBs of a 4 nm void in fcc Ni.

VII. Representative densities of major sinks

Representative densities of voids, dislocation loops, and SFTs as a function of temperature are obtained by linear regressions of the experimental data [6,7,13-24]. The representative density of SFTs, dislocation loops, and dislocations in irradiated Cu has been published in a previous work [25], the figure of which is shown in Fig. S11. The void density is also obtained by this work, as shown in Fig. S12. Specifically, the sink density, ρ_{sink}, decreases exponentially as the temperature (T) increases, the details of which are as follows:

$$\rho_{SFT}=10^{-0.014T+29.6}\ m^{-3}$$

$$\rho_{loop}=10^{-0.071T+25.6}\ m^{-3}$$

$$\rho_{dislocation}=10^{-0.0014T+13.8}\ m^{-2}$$

$$\rho_{void}=10^{-0.0074T+24.4}\ m^{-3}.$$

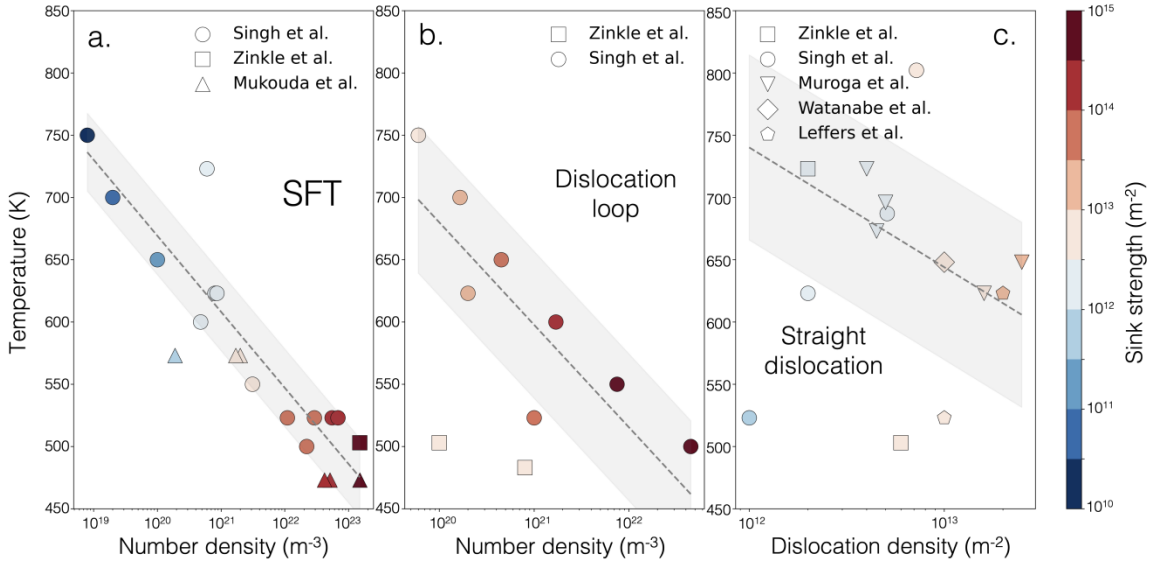

Fig. S11. Representative density of SFTs, dislocation loops, and straight dislocations in irradiated Cu, published by previous work [25].

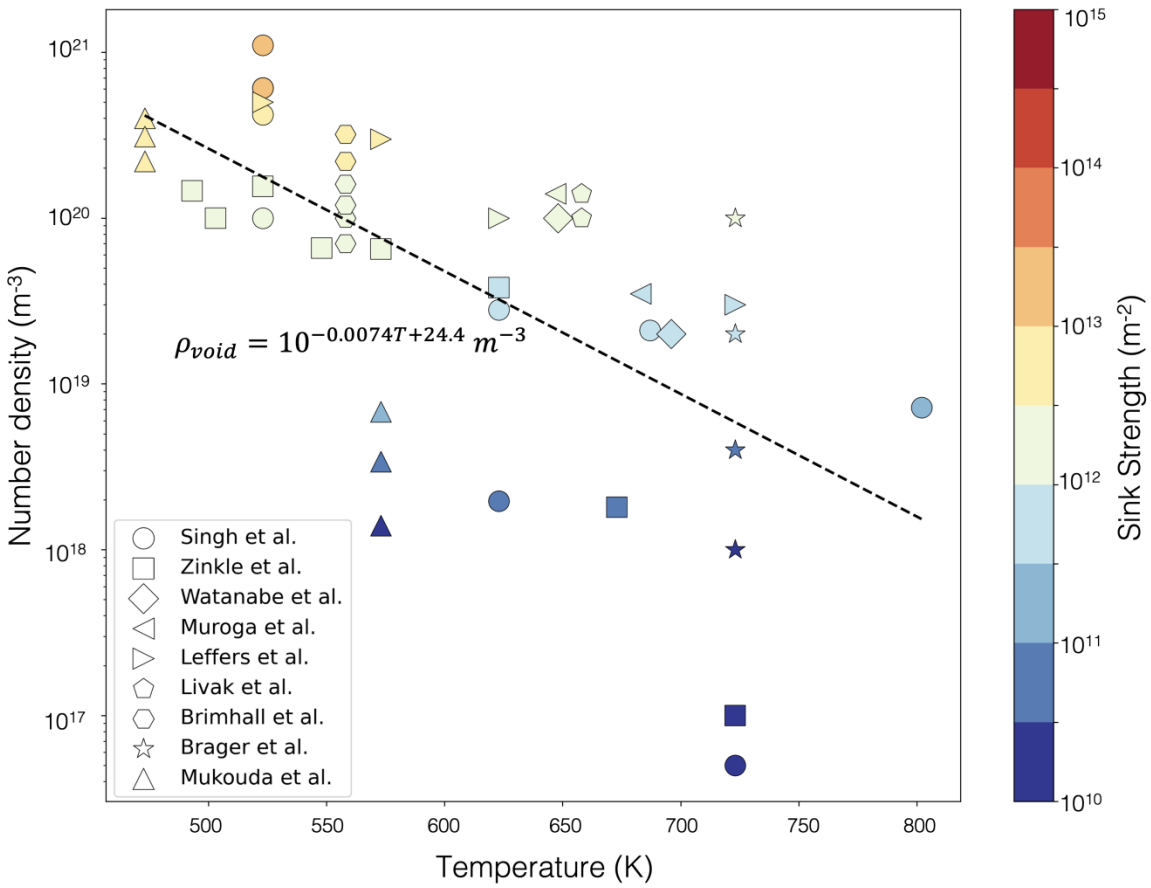

Fig. S12. Representative density of voids in irradiated Cu.

References

1. Xu, H.X.; Osetsky, Y.N.; Stoller, R.E. Self-evolving atomistic kinetic Monte Carlo: fundamentals and applications. *J Phys-Condens Mat* **2012**, *24*, doi:10.1088/0953-8984/24/37/375402.
2. Xu, H.X.; Stoller, R.E.; Beland, L.K.; Osetsky, Y.N. Self-Evolving Atomistic Kinetic Monte Carlo simulations of defects in materials. *Comp Mater Sci* **2015**, *100*, 135-143, doi:10.1016/j.commatsci.2014.12.026.
3. Bhattacharya, A.; Meslin, E.; Henry, J.; Barbu, A.; Poissonnet, S.; Decamps, B. Effect of chromium on void swelling in ion irradiated high purity Fe-Cr alloys. *Acta Mater* **2016**, *108*, 241-251, doi:10.1016/j.actamat.2016.02.027.
4. Borodin, V.A.; Volkov, A.E.; Ryazanov, A.I. The effect of bias factor variations on void nucleation in irradiated alloys. *J Nucl Mater* **2002**, *307*, 862-865, doi:10.1016/S0022-3115(02)01000-0.
5. Lee, T.S.; Hobbs, L.W.; Kohse, G.; Ames, M.; Harling, O.K.; Grant, N.J. Microstructural Evolution and Swelling of High-Strength, High Conductivity Rs-Pm Copper-Alloys Irradiated to 13.5 Dpa with Neutrons. *J Nucl Mater* **1986**, *141*, 179-183, doi:10.1016/S0022-3115(86)80032-0.

6. Muroga, T.; Yoshida, N. Microstructure of Neutron-Irradiated Copper Alloyed with Nickel and Zinc. *J Nucl Mater* **1994**, *212*, 266-269, doi:10.1016/0022-3115(94)90069-8.
7. Singh, B.N.; Horsewell, A.; Toft, P.; Edwards, D.J. Temperature and Dose Dependencies of Microstructure and Hardness of Neutron-Irradiated Ofhc Copper. *J Nucl Mater* **1995**, *224*, 131-140, doi:10.1016/0022-3115(95)00054-2.
8. Porollo, S.I.; Dvoriashin, A.M.; Vorobyev, A.N.; Konobeev, Y.V. The microstructure and tensile properties of Fe-Cr alloys after neutron irradiation at 400 degrees C to 5.5-7.1 dpa. *J Nucl Mater* **1998**, *256*, 247-253, doi:10.1016/S0022-3115(98)00043-9.
9. Zinkle, S.J.; Stoller, R.E. Quantifying defect production in solids at finite temperatures: Thermally-activated correlated defect recombination corrections to DPA (CRC-DPA). *J Nucl Mater* **2023**, *577*, doi:10.1016/j.jnucmat.2023.154292.
10. Golubov, S.I.; Barashev, A.V.; Stoller, R.E. Radiation Damage Theory. *Comprehensive Nuclear Materials, Vol 1: Basic Aspects of Radiation Effects in Solids/Basic Aspects of Multi-Scale Modeling* **2012**, 357-391.
11. Barashev, A.V.; Golubov, S.I.; Osetsky, Y.N.; Stoller, R.E. Dissociation of migrating particle from trap with long-range interaction field. *Philos Mag* **2010**, *90*, 907-921, doi:10.1080/14786430903193258.
12. Carpentier, D.; Jourdan, T.; Le Bouar, Y.; Marinica, M.C. Effect of saddle point anisotropy of point defects on their absorption by dislocations and cavities. *Acta Mater* **2017**, *136*, 323-334, doi:10.1016/j.actamat.2017.07.013.
13. Brager, H.R. Effects of Neutron-Irradiation to 63 Dpa on the Properties of Various Commercial Copper-Alloys. *J Nucl Mater* **1986**, *141*, 79-86, doi:10.1016/S0022-3115(86)80014-9.
14. Leffers, T.; Singh, B.N.; Buckley, S.N.; Manthorpe, S.A. Void-Swelling in Cold-Worked Copper during Hvem Irradiation. *J Nucl Mater* **1983**, *118*, 60-67, doi:10.1016/0022-3115(83)90179-4.
15. Livak, R.J.; Zocco, T.G.; Hobbs, L.W. Neutron Damage Microstructures of High-Conductivity Copper-Alloys. *J Nucl Mater* **1987**, *144*, 121-127, doi:10.1016/0022-3115(87)90287-X.
16. Mukouda, I.; Shimomura, Y. Damage evolution in neutron-irradiated Cu during neutron irradiation. *J Nucl Mater* **1999**, *271*, 230-235, doi:10.1016/S0022-3115(98)00710-7.
17. Singh, B.N.; Eldrup, M.; Horsewell, K.; Ehrhart, P.; Dworschak, F. On recoil energy dependent void swelling in pure copper - Part I. Experimental results. *Philos Mag A* **2000**, *80*, 2629-2650, doi:10.1080/01418610008216496.
18. Singh, B.N.; Eldrup, M.; Zinkle, S.J.; Golubov, S.I. On grain-size-dependent void swelling in pure copper irradiated with fission neutrons. *Philos Mag A* **2002**, *82*, 1137-1158, doi:10.1080/01418610208240021.
19. Singh, B.N.; Horsewell, A.; Gelles, D.S.; Garner, F.A. Void Swelling in Copper and Copper-Alloys Irradiated with Fission Neutrons. *J Nucl Mater* **1992**, *191*, 1172-1176, doi:10.1016/0022-3115(92)90659-9.
20. Singh, B.N.; Evans, J.H. Significant Differences in Defect Accumulation Behavior between Fcc and Bcc Crystals under Cascade Damage Conditions. *J Nucl Mater* **1995**, *226*, 277-285, doi:Doi 10.1016/0022-3115(95)00121-2.

21. Singh, B.N.; Leffers, T.; Horsewell, A. Dislocation and Void Segregation in Copper during Neutron-Irradiation. *Philos Mag A* **1986**, *53*, 233-242, doi:10.1080/01418618608242823.
22. Singh, B.N.; Zinkle, S.J. Defect Accumulation in Pure Fcc Metals in the Transient Regime - a Review. *J Nucl Mater* **1993**, *206*, 212-229, doi:10.1016/0022-3115(93)90125-I.
23. Zinkle, S.J.; Farrell, K. Void Swelling and Defect Cluster Formation in Reactor-Irradiated Copper. *J Nucl Mater* **1989**, *168*, 262-267, doi:10.1016/0022-3115(89)90591-6.
24. Zinkle, S.J.; Snead, L.L. Microstructure of Copper and Nickel Irradiated with Fission Neutrons near 230-Degrees-C. *J Nucl Mater* **1995**, *225*, 123-131, doi:10.1016/0022-3115(94)00670-9.
25. Yu, Z.; Lin, Y.R.; Zachman, M.J.; Zinkle, S.J.; Xu, H.X. The role of stacking fault tetrahedra on void swelling in irradiated copper. *Communications Materials* **2024**, *5*, doi:10.1038/s43246-024-00491-7.